RSC
Applied Interfaces

PAPER

View Article Online
View Journal | View Issue

Cite this: *RSC Appl. Interfaces*, 2024, **1**, 1001

Received 12th November 2023,
Accepted 26th April 2024

DOI: 10.1039/d3lf00220a

rsc.li/RSCApplInter

Large area van der Waals MoS_2–WS_2 heterostructures for visible-light energy conversion†

Matteo Gardella, [a] Giorgio Zambito, [a] Giulio Ferrando, [a] Francesco Bisio, [b] Maria Caterina Giordano *[a] and Francesco Buatier de Mongeot *[a]

In recent years, high-quality transition metal dichalcogenide layers and their van der Waals heterostructures, based on either mechanical exfoliation or chemical vapor deposition, have been successfully employed for the fabrication of electronic and optoelectronic devices, demonstrating their potential towards the integration or replacement of traditional semiconductor technologies. However, these fabrication techniques rely on single flakes with limited size on the scale of tens of micrometers. Here, we propose a large-scale growth process based on physical deposition that enables uniform coverage over cm^2 areas. This method allows us to fabricate a large area prototype van der Waals heterostructure by vertically stacking in sequence few-layer WS_2–MoS_2 films, forming a type-II heterojunction which shows enhanced photocatalytic dissociation efficiency compared to a reference MoS_2 film. Upon addition of a bottom graphene transparent electrode and a top Au contact, under illumination conditions we find evidence of photovoltage and photocurrent generation, thus demonstrating the potential of our large-scale 2D-TMD growth process in view of scalable, self-powered photoconversion applications.

Introduction

Bulk semiconductor photonics is the most widespread technology for photodetection and energy conversion thanks to the high efficiency of conventional semiconductor materials. However, new frontiers and challenges have been recently opened in materials science towards development of functional nanomaterials, such as organic materials and nanostructures, which could serve as flexible building blocks for the Internet of Things and wearable electronics.[1–6] To achieve the ambitious goal of a new generation of multi-functional devices and smart nanosensors, a crucial role is played by the emerging class of two-dimensional materials that exhibit exceptional optoelectronic response within atomically thin layers.[7–12]

Among these, transition metal dichalcogenides (TMDs) are 2D layered semiconductors of particular interest due to their thickness-dependent optoelectronic properties, with an indirect-to-direct band gap transition going from the bulk to a single monolayer.[13] Their high optical absorption coefficient, combined with suitable energy band gap values in the 1–2 eV range, makes them promising materials for photonics and photoconversion applications.[14–19]

Owing to the atomically smooth surfaces originating from in-plane fully saturated covalent bonds, TMDs as well as other two-dimensional materials can be vertically stacked to form the so-called van der Waals (vdW) heterostructures.[20–22] In such a configuration, novel properties emerge from the band structure coupling of the different layers, offering the possibility to arbitrarily tailor the optoelectronic properties of the resulting metamaterial.[23,24]

The possibility to devise ultra-thin self-powered photonic devices using 2D materials has been recently shown in van der Waals (vdW) metal–semiconductor–metal devices with engineered band alignment and in vdW MXene-silicon photodetectors.[25,26] Indeed, photon-to-current energy conversion in TMD-based heterostructures can be achieved at zero bias if the final energy band structure of the vdW 2D heterojunction intrinsically promotes the spatial separation of differently charged photoexcited carriers. A relevant example of this charge transfer effect has been recently demonstrated in the case of type-II vdW heterojunctions formed by MoS_2–WS_2, both in the monolayer regime and in the few- and multi-layer regime,[27–29] thanks to the staggered band alignment between the component layers.[30,31]

---

[a] Dipartimento di Fisica, Università di Genova, 16146 Genova, Italy.
E-mail: giordano@fisica.unige.it, buatier@fisica.unige.it
[b] CNR-SPIN, Corso Perrone 24, 16152 Genova, Italy

† Electronic supplementary information (ESI) available. See DOI: https://doi.org/10.1039/d3lf00220a

Additionally, charge separation leads to a longer lifetime of carriers, which can be exploited, for example, to enhance photocatalytic dissociation reactions of organic pollutants.[32,33] Since atomically thin 2D TMD films are endowed with an extremely high surface-to-volume ratio, it is thus straightforward to foresee the potential of large area TMD-based heterostructures in photo-to-chemical energy conversion applications.[34–36] Although the coupling of different TMD monolayers is particularly exciting for optoelectronic applications, in the case of van der Waals heterostructures based on few-layer TMDs, the increased thickness enables a higher optical absorption and hence an enhanced photoconversion efficiency.

Despite the photoconversion properties of these 2D materials being promising, the scalability of this scheme towards real-world devices is still very poor since the devices are typically based on exfoliated 2D semiconductor layers that form micrometric flakes. The limited size of these materials and their random distribution on the surface intrinsically limit the device area and require complex, low-throughput alignment procedures for the fabrication of vdW heterostructure devices at the micro-scale.[22]

To make real-world applications of TMD-based devices possible, development of scalable growth approaches is mandatory. Large area growth techniques are actively investigated, ranging from printable nanosheet inks in view of flexible and wearable electronics to chemical vapor deposition,[37–39] and a continuous effort is put in the search for wafer-scale homogeneous growth techniques with thickness control, enabling the application of 2D materials in circuit integration.[40–42] At the same time, development of large area transparent electrodes, such as those based on graphene, is crucial for the growth of van der Waals heterostructures and for the fabrication and interconnection of TMD-based devices.[43–45]

In this work, we develop large area physical deposition of 2D TMD films based on ion beam sputtering and recrystallization in a sulfur enriched atmosphere. In order to increase the weak photon absorption of monolayer thick TMD devices – in the 10% range – we opted for type-II heterojunctions formed from few-layer TMDs.[27–29] Vertical stacks of WS_2 and MoS_2 polycrystalline layers in a superstrate configuration are deposited on top of a commercial transparent conductive graphene electrode transferred on a silica (SiO_2) substrate. Upon illumination of the large area type-II heterojunction formed from the two TMD layers, we observe photovoltage and photocurrent. A further indirect experimental demonstration of the favorable band alignment is derived from photocatalytic dissociation of an organic pollutant such as methylene blue (MB). Indeed, due to the increased photocarrier lifetime resulting from physical separation of holes and electrons in type-II heterojunctions, the large area WS_2–MoS_2 stacked layers are more effective in promoting a higher MB photodissociation rate compared to the individual TMD layers. These results demonstrate the potential of our scalable approach for TMD-based van der Waals heterostructures in self-powered electronics.

Results and discussion

The controlled and deterministic growth of two-dimensional transition metal dichalcogenide semiconducting films extending over large area (cm^2 scale) represents one of the crucial bottlenecks which prevent real world applications based on van der Waals heterostructure devices. In our case, we chose WS_2 and MoS_2 TMD pairs which are characterized by a staggered alignment of the band edges (both in the monolayer regime and in the few-layer regime[27–29]) and thus form type-II heterojunctions which are at the core of self-powered photoconversion devices.

In view of light harvesting applications, we chose a transparent 12 × 25 mm^2 SiO_2 wafer as the supporting substrate. In order to electrically connect the TMD heterostructure on its back side and fabricate a large-scale device, we deposited a commercial bilayer graphene electrode (Graphenea) by a wet transfer process in deionized water, as highlighted in Fig. 1a and described in detail in ESI† section S1.[46] The graphene transparent electrode, which covers an area of about 1 cm^2, is evident in the photograph of the silica substrate. In Fig. 1b, we show the characteristic Raman spectrum of the graphene bilayer after the transfer process, highlighting the presence of characteristic vibrational modes located at 1589 cm^{-1} and 2690 cm^{-1}, which correspond to the G and 2D bands, respectively.[47] A very small peak can also be observed at 1350 cm^{-1} which is related to defects and disorder in the graphene layer. Its reduced area in comparison with the G and 2D bands indicates a high quality material.[48] Fig. 1c shows an optical extinction spectrum acquired on the as-transferred bilayer graphene. Extinction in the visible range is about 5%, in agreement with the expected theoretical absorption value of 4.6% for bilayer graphene.[49] The high

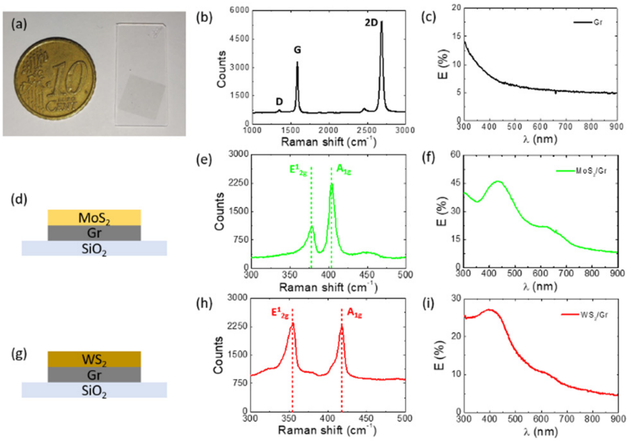

Fig. 1 a) Photograph of the transparent SiO_2 template after the transfer of a graphene bilayer conductive electrode. b) Raman spectrum of the graphene electrode after wet transfer on SiO_2. c) Optical extinction spectrum acquired on bilayer graphene. d) Sketch of a MoS_2–graphene–SiO_2 stack. e) Raman spectrum of MoS_2 on graphene. f) Optical extinction spectrum acquired on MoS_2 on graphene. g) Sketch of a WS_2–graphene–SiO_2 stack. h) Raman spectrum of the WS_2 film on graphene. i) Optical extinction spectrum acquired on WS_2 on graphene.

transparency of graphene is crucial for its application as a transparent window layer when photonic devices are arranged in a superstrate configuration.

Physical deposition of a few-layer MoS_2 film supported on a SiO_2–graphene stack (sketch in Fig. 1d) has been achieved by developing an ion beam sputtering deposition process from a stoichiometric MoS_2 target in an ultra high vacuum chamber (see the Methods section). To sequentially stack the different TMD layers, we designed a custom deposition set-up that allows the substrate to be oriented towards multiple TMD sputtering targets mounted on a linear translation stage (see ESI† section S2, Fig. S2a for more details). To optimize the quality of these TMD layers, which are amorphous after the deposition process, we perform a high temperature (750 °C) recrystallization process in a sulfur-enriched argon atmosphere to preserve their stoichiometry (see ESI† section S2, Fig. S2b). In this way, high-quality, 4 nm thick MoS_2 films in the semiconducting 2H-phase are formed, as demonstrated by the micro-Raman spectrum reported in Fig. 1e, which clearly shows the characteristic $E^1{}_{2g}$ and A_{1g} vibrational modes corresponding to the in-plane and out-of-plane vibrations of the molybdenum and sulfur sub-lattices, located at 378 cm^{-1} and 404 cm^{-1}, respectively.[50] The difference in the spectral positions of the two Raman peaks reads about 26 cm^{-1}, confirming the growth of a few-layer MoS_2 film.

Optical extinction measurements were performed across the UV-VIS-NIR spectral range on the same MoS_2–graphene sample. The results are presented in Fig. 1f. The spectrum acquired on the stacked MoS_2–graphene (green trace) highlights the presence of the characteristic excitonic features, which further confirm the formation of a 2H-MoS_2 semiconducting phase. A and B excitons are detected at about 677 nm and 629 nm, respectively, whereas the band nesting regions of C and D excitonic resonances are detected in the 400–450 nm spectral range.[51]

We used the same physical deposition approach for the large area growth of a 4 nm thick WS_2 film on top of a graphene layer (sketch in Fig. 1g). The micro-Raman spectrum reported in Fig. 1h shows the characteristic vibrational in-plane mode $E^1{}_{2g}$ and out-of-plane mode A_{1g} located at 354 cm^{-1} and 418 cm^{-1}, respectively, thus confirming the identification of a few-layer WS_2 film in the 2H-semiconducting phase.[52]

The optical extinction spectrum, reported in Fig. 1i, further supports the growth of few-layer WS_2 films in the semiconducting 2H-phase. The spectrum is characterized by the main excitonic features of WS_2 detected at about 630 nm (A exciton), 530 nm (B exciton, very shallow mode) and in the spectral range of 400–450 nm (C and D transitions of the band nesting region).[53] A comparison between the extinction spectrum of MoS_2 (Fig. 1f) and the spectrum of WS_2 (Fig. 1i) allows the strong similarity of the band structure of the two TMD materials to be highlighted in a direct manner, which are characterized by a very similar optical bandgap in the range of 1.3–1.4 eV for the few-layer regime.[54,55]

Having demonstrated the capability to grow by physical deposition the individual TMD and graphene layers placed deterministically on the silica wafer substrate, we then fabricated a large area van der Waals MoS_2–WS_2 heterostructure partly coating a transparent conductive graphene electrode by sequential deposition of a 4 nm thick WS_2 film and a 2 nm thick MoS_2 film, followed by a single recrystallization step at 750 °C (see ESI† section S2). According to the literature, with a WS_2 monolayer being 0.66 nm thick[56] and a MoS_2 monolayer being 0.65 nm thick,[57] we obtained a heterostructure based on six layers of WS_2 and three layers of MoS_2. Fig. 2a shows a photograph of the sample, where the graphene electrode is highlighted by the dashed blue rectangle. As a result, we achieved vertical stacking of graphene, WS_2 and MoS_2 layers over a 0.9 × 1.0 cm^2 area. The photograph also shows the two macroscopic Au metal electrodes deposited *via* ion beam sputtering to complete this large area prototype device. The two contacts are respectively located on the uncoated edge of the graphene electrode (back contact) and on the MoS_2–WS_2–graphene stack (top contact, which also acts as an optical reflector). A 2 nm thin Ti adhesion layer was added beneath the Au contacts by ion beam sputtering deposition. Cross section sketches of the vdW heterostructure device have been added to clarify the device geometry, designed for direct contact of graphene and for avoiding shunts between graphene and MoS_2. In the top sketch of Fig. 2a, a cross sectional view of the device along the horizontal direction (dashed black line) is represented, showing the vertical stacking of graphene, WS_2 and MoS_2. The left sketch, on the other hand, represents a cross sectional view of the device along the vertical direction (dashed red line). In the sketch, we do not include the 2 nm Ti adhesion layer between Au and MoS_2 since the drawing is already intricated. The adopted geometry with vertical stacking of polycrystalline TMD layers and electrodes takes its cue from conventional design of polycrystalline photovoltaic devices and is particularly advantageous because it

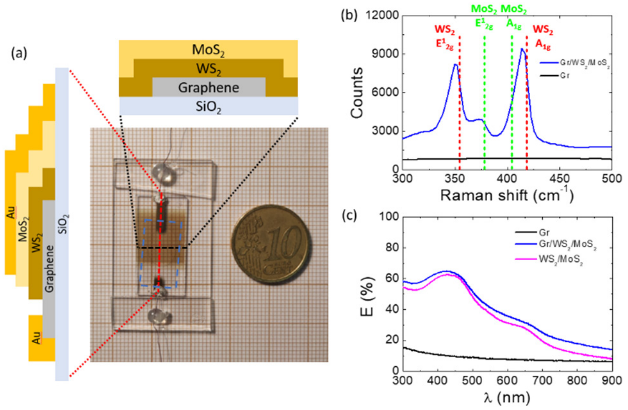

Fig. 2 a) Photograph of a large area van der Waals heterojunction composed of a stack of graphene (dashed blue rectangle), WS_2 and MoS_2. The top sketch represents a cross-section across the heterostructure stack along the horizontal direction (black trace), the side sketch represents a cross-section across along the vertical direction (red trace). b) Raman spectra acquired in the heterojunction region (blue trace) and on the bare graphene (black trace). c) Optical extinction spectra acquired on bare graphene (black trace), on WS_2–MoS_2 on top of graphene (blue trace) and on WS_2–MoS_2 outside the graphene (magenta trace).

selects charge transport in the vertical direction across single crystalline TMD domains (typical sizes of crystalline domains determined by TEM on similar TMD samples are in the range of 30–40 nm (ref. 39)). Conversely, charge transport across lateral heterojunctions would suffer from increased resistance at the grain boundaries of the polycrystalline TMD films.

Fig. 2b presents the Raman characterization of the TMD heterostructure, showing a spectrum acquired on the vertically stacked MoS_2 and WS_2 layers (blue trace). The dashed lines have been added to the graph to help identify the spectral fingerprints belonging to the individual MoS_2 (green) and WS_2 (red) layers. The Raman spectrum of the TMD heterostack shows the presence of the well separated $E^1{}_{2g}$ modes corresponding to WS_2 and MoS_2, and of the A_{1g} modes which are partly overlapped, thus confirming that the thermal annealing process is effective in recrystallizing also the WS_2 layer buried below the MoS_2 layer. The Raman spectrum acquired on the bare graphene, close to the Au back contact (black trace), shows no spectral fingerprints of TMDs, hence demonstrating that the physical deposition process here described enables on-demand deposition of 2D TMD semiconducting layers with a deterministic geometry defined by a proximity stencil mask. This is at variance with TMD deposition achieved by conventional CVD procedures, which results in the growth of randomly nucleated flakes.[58]

This approach is advantageous in the more general context of photocatalytic applications, where a key goal is to achieve a single-step and scalable synthesis of large area MoS_2/WS_2 heterostacks independently from the interconnection to top and bottom contacts. The robustness of our physical growth technique is confirmed by the experimental evidence shown in ESI† section 3.

Fig. 2c reports the extinction spectrum acquired in correspondence to the vertically stacked MoS_2–WS_2–graphene van der Waals heterostructure (blue trace) shown in Fig. 2a and b. A direct comparison with the extinction spectra of bare graphene (black) and WS_2–MoS_2 stacked layers without graphene (magenta) confirms that the graphene bilayer does not contribute with relevant spectral features to the observed extinction. Due to the spectral overlap of the dominant excitonic features of the individual TMD layers, the optical response of the vertical heterostructure does not clearly resolve the individual components shown in Fig. 1. In view of photoconversion applications, we highlight the substantial increase in the optical extinction with respect to the individual TMD layers, exceeding 60% in correspondence to the band nesting region (C, D excitons around 400 nm) and reaching 30% in correspondence to the A exciton (optical transitions around 650 nm).

The optoelectronic response of this large area heterostructure device has been investigated by photovoltage and photocurrent measurements under controlled illumination conditions, with the light beam impinging from the side of the transparent silica support (superstrate configuration). Due to the type-II band structure of the TMD pair, the built-in voltage is expected to promote vertical separation of the photogenerated charges of opposite sign across the van der Waals interface.[27–29] The effective active area of the TMD heterostructure, where vertical transport occurs, is determined by the top Au/Ti contact defined by sputtering deposition through a proximity mask. In the current implementation, the top contact active area approximately spans across 2 × 4 mm^2. However, we emphasize that for the heterostructure shown in Fig. 2a, the active area could be easily scaled up by enlarging the Au top electrode area to entirely cover the region of the graphene back contact coated by the TMD stack. We further highlight that the currently achievable size of the TMD heterostructures is only limited by the lab-scale prototype set-up employed for ion beam sputtering deposition and by the size of the transferred graphene back contact. Straightforward scalability at the wafer level (4″ and beyond) is at hand since no fundamental constraints of the TMD physical deposition process are foreseen and larger CVD graphene layers can be transferred on demand.

In a first set of photoconversion experiments, a collimated broadband halogen light source covering the vis-NIR spectral range was employed to illuminate the active area of the van der Waals heterojunction. Fig. 3a reports the photovoltage $V_{OC}(t)$ acquired under open-circuit conditions as a function of time under alternating on–off illumination conditions, and for different illumination power density levels as measured by a thermopile power meter (see the Methods section for further details). The voltage response of the TMD heterojunction follows a first-order trend, with a characteristic time constant τ of about 16 seconds, as shown in more detail in ESI† section S3.

In a second run of measurements, performed under steady illumination conditions, we detect the photovoltage saturation value $V_{OC,ss}$ finding a linear trend as a function of the incident optical power, as demonstrated by the plot in Fig. 3b. An open-circuit photovoltage as high as 40 μV is measured for homogeneous illumination of the device at an optical intensity of 252 mW cm^{-2}. A blue bar is added to the graph to highlight the noise level of the measurements.

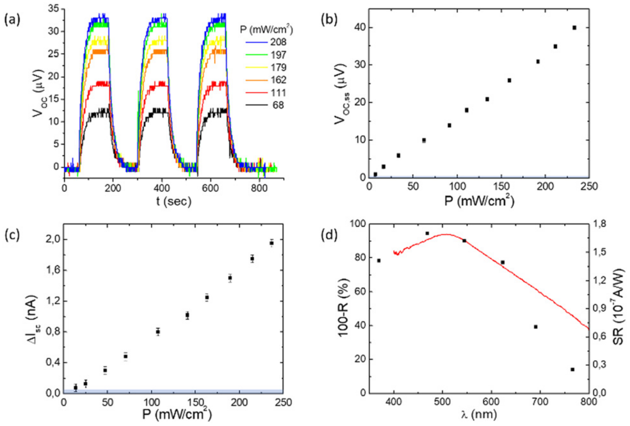

Fig. 3 a) Time-dependent open circuit photovoltage response $V_{OC}(t)$ under broadband illumination at different powers. b and c) Steady state photovoltage $V_{OC,ss}$ and net photocurrent ΔI_{SC} under stationary conditions as a function of incident power. d) Comparison between optical absorption and spectral responsivity.

In a similar way, the net short-circuit photocurrent ΔI_{SC} was measured at different stationary illumination power levels. The results reported in Fig. 3c show an approximately linear dependence of ΔI_{SC} from the illumination power density P, with a net photocurrent increase of up to 2 nA in correspondence to the optical power density P = 236 mW cm^{-2}. As with the photovoltage, the blue bar in the graph indicates the noise level after subtraction of a 0.4 nA offset determined under dark conditions.

To evaluate the spectral responsivity of the device under monochromatic illumination conditions, a monochromatized xenon light source was employed for photoexcitation under stationary illumination conditions at different wavelengths λ, spanning from about 470 nm to 770 nm. The optical power density $P(\lambda)$ was acquired with a calibrated photodiode power meter. The current/power spectral responsivity $\mathrm{SR}(\lambda) = \Delta I_{SC}(\lambda)/P(\lambda)$, derived from the measured short circuit photocurrent and the optical power, is plotted in Fig. 3d (black squares). The spectral responsivity sharply increases as the wavelength decreases from the near-IR across the TMD optical bandgap. This corresponds to the spectral region of excitonic transitions where optical absorption is higher.

In an independent way, we determine the spectral dependence of optical reflectivity $R(\lambda)$ of the TMD heterostructure using a reflection/backscattering fibered probe. Since the reflectivity measurement is performed by illuminating from the SiO_2 side, in correspondence to the Au contact which acts as a back-reflector, light transmission and scattering from the flat interfaces can be neglected and spectral absorption $A(\lambda)$ can be derived from the reflection spectrum according to $A(\lambda) = 100\% - R(\lambda)$. The maximum of the absorption spectrum plotted in Fig. 3d (red line) is found at around 500 nm wavelength and closely matches the spectral trend of the current/power spectral responsivity.

The observation of a net photocurrent and photovoltage in our proof-of-concept large area TMD heterojunction provides an indirect confirmation of a type-II band alignment which is required for self-powered photoconversion, in agreement with previous reports on few-layer TMD heterojunctions pairs.[28,29] The conduction band minimum (CBM) and valence band maximum (VBM) energy levels of TMDs are dependent on the number of layers. Generally speaking, as the number of layers is reduced, the VBMs of all TMDs move downward (lower in energy), whereas the CBMs move upward (higher in energy), both of which can be understood on the basis of quantum confinement arguments. First-principles and DFT evaluations of TMD energy bands show that WS_2–MoS_2 heterojunctions have a type-II band alignment both in the monolayer regime and in the bulk regime.[59] In the specific case of our heterostructure (6ML WS_2/3ML MoS_2), from the layer-dependent TMD band calculations reported in ref. 60 we can derive that CMBs read −4.06 eV and −4.34 eV for WS_2 and MoS_2, respectively, while VBMs read −5.05 eV and −5.40 eV. This corresponds to a valence band offset of 0.34 eV and a conduction band offset of 0.29 eV, as expected for type-II heterostructures.

A straightforward comparison of the electro-optical performance of MoS_2/WS_2 heterostructure devices based on univocal efficiency/performance parameters is a non-trivial task due to the strong dissimilarity of the fabrication procedures (exfoliated flakes *vs.* large area techniques), device area, illumination conditions, *etc.*, as listed in ref. 61 and in more recent references.[27,62–68]

We also stress that the absolute photocurrent and photovoltage values which have been measured in our proof-of-concept TMD heterojunction are far too low for any realistic electro-optical photoconversion application. This limitation is primarily due to the very high series resistance of the graphene bilayer back contact, in the range of 20 kΩ (more details in ESI† section S4). In fact, if we consider a simple Shockley equivalent circuit of the heterojunction, the high parasitic resistance forward polarizes the inner junction responsible for recombination in the TMD material, thus hampering the photocurrent and photovoltage output.[69] Further developments, which go beyond the scope of our paper, will require optimization of the back transparent conductive contact since optimization of graphene transfer and of the TMD growth process can reduce graphene sheet resistance, which contributes to the photovoltage and photocurrent deterioration.

Concerning the top Au/Ti/MoS_2 contact, we also notice that band structure calculations and experimental data for ideal TMD layers produced by exfoliation, highlight the presence of an additional Schottky barrier which hinders charge injection efficiency.[70,71] However, when contacts are made between more defective MoS_2 interfaces, such as those produced by CVD, and Ti/Au electrodes are obtained by more energetic sputtering deposition, the Schottky barrier is substantially lowered due to the higher density of interface defects, and the metallization of the MoS_2/Au contact is effective.[72–74] The latter conditions apply to our case since both MoS_2 and metal contacts are deposited by sputtering, nevertheless future efforts to further optimize the top contact could exploit semimetals (Bi and Sb for example)[75,76] or other electrodes like indium alloy.[77,78]

Independently from the optimization of the electro-optical parameters, the possibility to vertically stack the TMD layers by physical deposition methods which are scalable to the wafer-level proves crucial in view of large area applications, such as photocatalytic water splitting and water remediation.[34] In these applications, the overall throughput and efficiency are affected by the active semiconductor area. Additionally, the type-II heterojunction configuration promotes photo-induced charge separation and boosts the absorption of solar light from UV to visible light, leading to improved efficiency.[36,79]

Here, as a case study, we studied the photobleaching reaction of methylene blue (MB), a polluting organic molecule commonly employed as fabric dye or as a pharmaceutical, in the presence of different TMD samples immersed in MB solution. We fabricated a bilayer heterostack composed of a thicker WS_2 layer (12 nm) coated by a thinner MoS_2 outer layer (2 nm) and compared its photocatalytic performance with that of an individual 8 nm thick

MoS_2 reference layer, with an average optical absorption comparable to the WS_2–MoS_2 heterostack. We also compared the reactivity with that of an individual 12 nm thick WS_2 reference layer (the same thickness as in the heterostack).

The experimental set-up is sketched in Fig. 4a: a cuvette containing the MB solution and the TMD sample is illuminated by monochromatized light together with a blank reference cuvette containing only the MB solution. In Fig. 4b, the optical transmission spectrum for the initial MB solution at a concentration $C_0 = 1.3 \times 10^{-5}$ mol L^{-1} is reported (blue curve). A double dip is observed in the spectral region from 550 nm to 700 nm, corresponding to the characteristic absorption peaks of MB.[80] Almost full transmittance is observed for shorter and longer wavelengths, respectively. By monitoring the different evolution of MB concentration as a function of the photon exposure dose in the case of different TMD samples, it is then possible to evaluate the photocatalytic performance of the samples (see the Methods section and ESI† section 6 for further details).

Fig. 4b also reports the optical transmission spectra of different TMD samples. The red curve represents the optical transmission of the bilayer heterostack. The optical spectrum is dominated by the spectral features of the thicker WS_2 layer, showing the characteristic excitonic modes at 630 nm (A exciton) and 540 nm (B exciton) and the band nesting region in the 400–450 nm spectral region. Finally, the green line refers to the individual MoS_2 sample transmission spectrum and shows the characteristic A and B excitons (at 675 nm and 625 nm, respectively) and the band nesting region at 400–450 nm. As already mentioned, the thickness of the MoS_2 layer has been chosen in order to achieve equivalent optical absorption to the heterostack, and in turn a similar density of photogenerated charges in the two samples. Since the MB solution is in contact with the same MoS_2 outer surface in both cases, and with the optical absorption in the two samples being comparable, we can infer the contribution of charge separation in the type-II heterojunctions from the difference in photocatalytic performances between the two samples.

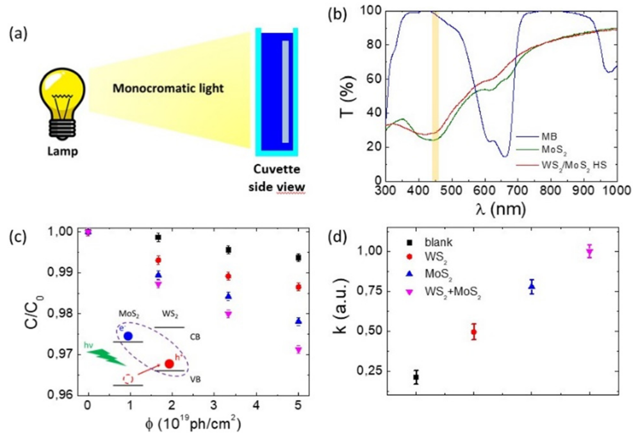

Fig. 4 a) Scheme of the set-up employed for photobleaching experiments. b) Transmission spectra for the initial MB solution, the MoS_2–WS_2 heterostack sample and a MoS_2 sample with an optical thickness equivalent to the heterostack. The yellow bar indicates the exposure wavelength. c) MB solution concentration as a function of exposure dose for illumination with monochromatic light at λ = 450 nm using different photocatalysts. A schematic of the type-II band alignment of the MoS_2–WS_2 heterostructure, favoring charge separation of electrons and holes, is shown in the inset. d) Kinetic constant k of MB photodissociation for different TMD samples, expressed in arbitrary units. The values are normalized to the most reactive sample.

For the MB photobleaching experiments, we illuminated the cuvettes containing the MB solution and the TMD samples with monochromatized light at a wavelength of 450 nm (25 nm bandwidth). As shown by the yellow band in the transmission spectra in Fig. 4b, such a wavelength on one side ensures the maximum reactivity from the TMD samples in correspondence to the band nesting region, where the optical absorption is higher, and at the same time reduces MB self-degradation because the molecule weakly absorbs light in the selected spectral region.

The results of the MB photodegradation experiments are reported in Fig. 4c. The black squares represent the decrease in MB concentration due to self-bleaching under illumination when no TMD is added as a photocatalyst. The red circles and blue triangles describe the experiments in the presence of pure WS_2 and MoS_2 layers, respectively. Both TMD pure layers promote photodegradation, which is comparatively stronger in the MoS_2 case.[81] Finally, the purple triangles describe the photobleaching experiment in the case of the MoS_2–WS_2 heterojunction, evidencing that the MB degradation rate is the highest among the possible TMD configurations, *i.e.* a factor 2.0 higher than for WS_2 and 1.3 higher than for MoS_2 films of comparable active area. Comparison with the latter sample is particularly relevant since they have in common the same MoS_2 outer interface, which determines an equivalent surface chemistry. Since the optical extinction of the two samples at 450 nm wavelength is comparable (Fig. 4b), it is possible to directly evaluate the enhancement of MB photobleaching induced by the van der Waals heterostructure.[82] The type-II band alignment of the WS_2 and MoS_2 layers (sketch in the inset of Fig. 4c) in fact ensures a longer lifetime of the photogenerated carriers in the case of the heterostructure, since the built-in field at the interface drives spatial separation of electrons towards MoS_2 and holes towards WS_2.[83]

To compare more quantitatively the photocatalytic activity of the samples, we calculate the kinetic constant k according to the first order reaction kinetic law, where C is the MB concentration as a function of the time t and C_0 is the concentration of MB at the beginning of the exposure. Due to the low photon doses used, the exponential law can be approximated to first order by a linear law as reported in ESI† Fig. S7. In Fig. 4d, we plot the kinetic constants evaluated for the different samples, concluding that the WS_2–MoS_2 stack is significantly more reactive compared to both a layer of WS_2 and MoS_2.

The observed enhanced photobleaching from TMD heterostructures is in qualitative agreement with the electro-optical measurements demonstrating photocurrent and photovoltage, and both stem from the type-II band alignment of the TMD pair which makes self-powered photoconversion applications possible.

In view of prospective alternative applications, the more general impact and scalability of our approach for the fabrication of large area TMD-devices are also derived from the possibility to grow TMD heterojunctions based on different chalcogens, *e.g.* selenides[84] or tellurides.[85] This would require (i) switching to a different TMD sputtering target for the physical deposition of the TMD solid precursor film and (ii) optimizing the recrystallization in a chalcogenide atmosphere using a dedicated tubular furnace.

Conclusions

In summary, we demonstrate a physical deposition approach of large area TMD films based on ion beam sputtering from stoichiometric TMD targets. This method can be tailored for the deposition of large area MoS_2 and WS_2 films in the few-layer regime. We further demonstrate that sequential deposition of the two TMD precursor films enables vertical stacking of a large area MoS_2–WS_2 heterostructure supported onto a transparent graphene electrode in a single step. Our custom lab-scale setup enables deposition of samples at the cm^2 level, but the process is scalable at the wafer level employing currently available industrial deposition facilities. Under illumination conditions across the proof-of-concept heterostructure device, we measure a net photovoltage and photocurrent, although absolute values are limited by the very high parasitic series resistance of the commercial graphene electrode. However, the observations independently support the type-II band alignment of the TMD hetero-stack which can be exploited for instance in photocatalytic applications, which do not require optimization of the back contact series resistance or connection to an external circuit. In a further set of experiments, we demonstrate that the large area MoS_2–WS_2 heterostructure platforms effectively enhance the photodissociation rate of methylene blue test molecules compared to individual TMD layers with similar optical absorbance and surface chemistry. These results highlight the potential of the scalable physical deposition approach to obtain vertically stacked TMD heterostructures, which hold promise for large-scale and self-powered energy conversion applications that exploit type-II band alignment and efficient charge separation.

Methods

TMD and top contact deposition

A custom-made ultra high vacuum chamber is equipped with an ion gun (ECR plasma source TPIS by TECTRA). The chamber is pumped down to 10^{-7}–10^{-6} mbar by means of rotary and turbomolecular pumps and filled with argon (up to 6.0×10^{-4} mbar). A plasma is then generated by the ion gun magnetron and the ions are extracted by the use of two grids set at different electrostatic potentials, generating a 1.44 keV Ar^+ ion beam (gas purity N5.0). The as-formed directional ion beam is used to sputter a TMD target, from which the material is deposited on the desired substrate. A quartz crystal microbalance is used to monitor deposition flux and thickness, which is calibrated by means of atomic force microscopy measurements on lithographic nanostructures.

Deposition of the top contacts proceeds under the same experimental conditions *via* ion beam sputtering deposition, employing as targets Ti and Au foil of high purity.

Raman characterization

Raman micro-spectra were acquired either by using an NRS-4100 Raman microscope (JASCO) operating in the back-scattering configuration equipped with a 100× objective and a 532 nm laser source, or by using a Horiba Raman XploRA microscope in the same configuration.

Optical characterization

The optical response was investigated by normal incidence transmission set-up extinction spectroscopy. The samples were illuminated using a halogen-deuterium lamp (DH-2000-BAL, Mikropak) coupled to an optical fiber with a core diameter of 600 μm and the transmitted light was fiber-coupled to an Ocean Optics (HR4000) spectrometer. The data were normalized to the silica substrate transmittance.

Optoelectronic characterization

A collimated broadband halogen light source (Osram 64 255 8 V 20 W) covering the vis-NIR spectral range was employed to illuminate the active area of the van der Waals heterojunction. The photovoltage $V_{OC}(t)$ was acquired under open-circuit conditions with an HP 3478A Multimeter, as a function of time under alternating on–off illumination conditions, and for different illumination power density levels as measured with a thermopile power meter (Scientech Astral AI310). In a similar way, the net short circuit photocurrent ΔI_{SC} was measured at different stationary illumination power levels, by using a Keithley 6487 picoammeter/voltage source connected to the two terminals of the TMD heterostructure device.

Photodegradation experiments

The experimental set-up is composed of a xenon light source (Newport TLS130B-300X) that can be monochromatized by a grating spectrometer. The photon exposure dose is calibrated using a photodiode power meter (Newport Power Meter Model 1919-R).

The concentration evolution of MB molecules in water solution ($C_0 = 1.3 \times 10^{-5}$ mol L^{-1}) as a function of the photon exposure dose is evaluated by measuring the characteristic transmittance of the solution in a quartz cuvette at a wavelength of 660 nm, in correspondence to the maximum of MB absorbance (see ESI† section S6 for more details).

Exposures are performed under monochromatic illumination at 450 nm (see ESI† section S6 for more details).

Conflicts of interest

There are no conflicts to declare.

Acknowledgements

Technical assistance from R. Chittofrati and E. Vigo is acknowledged. We acknowledge M. Scambelluri of Laboratorio Raman at Department DISTAV, Università degli Studi di Genova, for assistance in the Raman measurements with the Horiba set-up. F. B. and G. Z. acknowledge Fondazione San Paolo for project Panlab and PhD scolarship. F. B. d. M. and M. C. G. acknowledge financial support from Ministero dell'Università e della Ricerca, within the project "Dipartimento di Eccellenza 2018–2022" art. 1, c. 314–337, Legge 232/2016. F. B. d. M. acknowledges financial support from Università degli Studi di Genova within the project BIPE 2020. M. C. G. acknowledges financial support from Ministero degli Affari Esteri e della Cooperazione Internazionale (MAECI) within "Progetti di Grande Rilevanza 2021–2023" – bilateral project Italy–Vietnam "Large-area 2D/plasmonic heterostructures for photocatalysis and energy storage (H2D)". F. B. d. M. and M. C. G. acknowledge support from Ministero dell'Università e della Ricerca (MUR), Project funded under the National Recovery and Resilience Plan (NRRP), Mission 4 Component 2 Investment 1.3 – Call for tender No. 1561 of 11.10.2022; funded by the European Union – NextGenerationEU • Award Number: Project code PE0000021, Concession Decree No. 1561 of 11.10.2022 adopted by Ministero dell'Università e della Ricerca (MUR), CUP D33C22001300002 Project title "Network 4 Energy Sustainable Transition – NEST". F. B. d. M. acknowledges support from Ministero dell'Università e della Ricerca (MUR), project PRIN2022 "2022FWB2HE". M. C. G. acknowledges support from "Progetto Curiosity Driven 2021", funded by the European Union – NextGenerationEU. F. B. d. M. acknowledges support from MASE (Ministero dell'Ambiente e della Sicurezza Energetica) in the framework of the Operating Agreements with ENEA for Research on the Electric System.

References

1 S. Qiang, T. Carey, A. Arbab, W. Song, C. Wang and F. Torrisi, Wearable Solid-State Capacitors Based on Two-Dimensional Material All-Textile Heterostructures, *Nanoscale*, 2019, **11**(20), 9912–9919, DOI: **10.1039/C9NR00463G**.

2 G. R. Bhimanapati, Z. Lin, V. Meunier, Y. Jung, J. Cha, S. Das, D. Xiao, Y. Son, M. S. Strano, V. R. Cooper, L. Liang, S. G. Louie, E. Ringe, W. Zhou, S. S. Kim, R. R. Naik, B. G. Sumpter, H. Terrones, F. Xia, Y. Wang, J. Zhu, D. Akinwande, N. Alem, J. A. Schuller, R. E. Schaak, M. Terrones and J. A. Robinson, Recent Advances in Two-Dimensional Materials beyond Graphene, *ACS Nano*, 2015, **9**(12), 11509–11539, DOI: **10.1021/acsnano.5b05556**.

3 A. M. Hussain and M. M. Hussain, CMOS-Technology-Enabled Flexible and Stretchable Electronics for Internet of Everything Applications, *Adv. Mater.*, 2016, **28**(22), 4219–4249, DOI: **10.1002/adma.201504236**.

4 F. Yi, H. Ren, J. Shan, X. Sun, D. Wei and Z. Liu, Wearable Energy Sources Based on 2D Materials, *Chem. Soc. Rev.*, 2018, **47**(9), 3152–3188, DOI: **10.1039/C7CS00849J**.

5 L. Fichera, G. Li-Destri and N. Tuccitto, Fluorescent Nanoparticle-Based Internet of Things, *Nanoscale*, 2020, **12**(17), 9817–9823, DOI: **10.1039/D0NR01365J**.

6 Y. Pang, Z. Yang, Y. Yang and T. Ren, Wearable Electronics Based on 2D Materials for Human Physiological Information Detection, *Small*, 2020, **16**(15), 1901124, DOI: **10.1002/smll.201901124**.

7 H. Singh Nalwa, A Review of Molybdenum Disulfide(MoS_2) Based Photodetectors: From Ultra-Broadband, Self-Powered to Flexible Devices, *RSC Adv.*, 2020, **10**(51), 30529–30602, DOI: **10.1039/D0RA03183F**.

8 W. Choi, N. Choudhary, G. H. Han, J. Park, D. Akinwande and Y. H. Lee, Recent Development of Two-Dimensional Transition Metal Dichalcogenides and Their Applications, *Mater. Today*, 2017, **20**(3), 116–130, DOI: **10.1016/j.mattod.2016.10.002**.

9 J. Cherusseri, N. Choudhary, K. S. Kumar, Y. Jung and J. Thomas, Recent Trends in Transition Metal Dichalcogenide Based Supercapacitor Electrodes, *Nanoscale Horiz.*, 2019, **4**(4), 840–858, DOI: **10.1039/C9NH00152B**.

10 C. Martella, C. Mennucci, A. Lamperti, E. Cappelluti, F. B. de Mongeot and A. Molle, Designer Shape Anisotropy on Transition-Metal-Dichalcogenide Nanosheets, *Adv. Mater.*, 2018, **30**(9), 1705615, DOI: **10.1002/adma.201705615**.

11 A. Genco and G. Cerullo, Optical Nonlinearity Goes Ultrafast in 2D Semiconductor-Based Nanocavities, *Light: Sci. Appl.*, 2022, **11**(1), 127, DOI: **10.1038/s41377-022-00827-3**.

12 M. Bhatnagar, M. C. Giordano, C. Mennucci, D. Chowdhury, A. Mazzanti, G. Della Valle, C. Martella, P. Tummala, A. Lamperti, A. Molle and F. Buatier de Mongeot, Ultra-Broadband Photon Harvesting in Large-Area Few-Layer MoS_2 Nanostripe Gratings, *Nanoscale*, 2020, **12**(48), 24385–24393, DOI: **10.1039/D0NR06744J**.

13 S. Manzeli, D. Ovchinnikov, D. Pasquier, O. V. Yazyev and A. Kis, 2D Transition Metal Dichalcogenides, *Nat. Rev. Mater.*, 2017, **2**(8), 17033, DOI: **10.1038/natrevmats.2017.33**.

14 D. Maeso, A. Castellanos-Gomez, N. Agraït and G. Rubio-Bollinger, Fast Yet Quantum-Efficient Few-Layer Vertical MoS_2 Photodetectors, *Adv. Electron. Mater.*, 2019, **5**(7), 1900141, DOI: **10.1002/aelm.201900141**.

15 C. Palacios-Berraquero, D. M. Kara, A. R.-P. Montblanch, M. Barbone, P. Latawiec, D. Yoon, A. K. Ott, M. Loncar, A. C. Ferrari and M. Atatüre, Large-Scale Quantum-Emitter Arrays in Atomically Thin Semiconductors, *Nat. Commun.*, 2017, **8**(1), 15093, DOI: **10.1038/ncomms15093**.

16 D. Jariwala, A. R. Davoyan, J. Wong and H. A. Atwater, Van Der Waals Materials for Atomically-Thin Photovoltaics: Promise and Outlook, *ACS Photonics*, 2017, **4**(12), 2962–2970, DOI: **10.1021/acsphotonics.7b01103**.

17 M. Bhatnagar, M. Gardella, M. C. Giordano, D. Chowdhury, C. Mennucci, A. Mazzanti, G. D. Valle, C. Martella, P. Tummala, A. Lamperti, A. Molle and F. Buatier de Mongeot,

Broadband and Tunable Light Harvesting in Nanorippled MoS_2 Ultrathin Films, *ACS Appl. Mater. Interfaces*, 2021, **13**(11), 13508–13516, DOI: 10.1021/acsami.0c20387.

18 T. Bucher, A. Vaskin, R. Mupparapu, F. J. F. Löchner, A. George, K. E. Chong, S. Fasold, C. Neumann, D.-Y. Choi, F. Eilenberger, F. Setzpfandt, Y. S. Kivshar, T. Pertsch, A. Turchanin and I. Staude, Tailoring Photoluminescence from MoS_2 Monolayers by Mie-Resonant Metasurfaces, *ACS Photonics*, 2019, **6**(4), 1002–1009, DOI: 10.1021/acsphotonics.8b01771.

19 J. F. Gonzalez Marin, D. Unuchek, K. Watanabe, T. Taniguchi and A. Kis, MoS2 Photodetectors Integrated with Photonic Circuits, *npj 2D Mater. Appl.*, 2019, **3**(1), 14, DOI: 10.1038/s41699-019-0096-4.

20 A. K. Geim and I. V. Grigorieva, Van Der Waals Heterostructures, *Nature*, 2013, **499**(7459), 419–425, DOI: 10.1038/nature12385.

21 K. S. Novoselov, A. Mishchenko, A. Carvalho and A. H. Castro Neto, 2D Materials and van Der Waals Heterostructures, *Science*, 2016, **353**(6298), aac9439, DOI: 10.1126/science.aac9439.

22 H. Qi, L. Wang, J. Sun, Y. Long, P. Hu, F. Liu and X. He, Production Methods of Van Der Waals Heterostructures Based on Transition Metal Dichalcogenides, *Crystals*, 2018, **8**(1), 35, DOI: 10.3390/cryst8010035.

23 C. Trovatello, G. Piccinini, S. Forti, F. Fabbri, A. Rossi, S. De Silvestri, C. Coletti, G. Cerullo and S. Dal Conte, Ultrafast Hot Carrier Transfer in WS2/Graphene Large Area Heterostructures, *npj 2D Mater. Appl.*, 2022, **6**(1), 24, DOI: 10.1038/s41699-022-00299-4.

24 J.-S. Kim, N. Maity, M. Kim, S. Fu, R. Juneja, A. Singh, D. Akinwande and J.-F. Lin, Strain-Modulated Interlayer Charge and Energy Transfers in MoS_2/WS_2 Heterobilayer, *ACS Appl. Mater. Interfaces*, 2022, **14**(41), 46841–46849, DOI: 10.1021/acsami.2c10982.

25 C. Zhou, S. Zhang, Z. Lv, Z. Ma, C. Yu, Z. Feng and M. Chan, Self-Driven WSe2 Photodetectors Enabled with Asymmetrical van Der Waals Contact Interfaces, *npj 2D Mater. Appl.*, 2020, **4**(1), 46, DOI: 10.1038/s41699-020-00179-9.

26 Z. Kang, Y. Ma, X. Tan, M. Zhu, Z. Zheng, N. Liu, L. Li, Z. Zou, X. Jiang, T. Zhai and Y. Gao, MXene-Silicon Van Der Waals Heterostructures for High-Speed Self-Driven Photodetectors, *Adv. Electron. Mater.*, 2017, **3**(9), 1700165, DOI: 10.1002/aelm.201700165.

27 N. Huo, J. Kang, Z. Wei, S.-S. Li, J. Li and S.-H. Wei, Novel and Enhanced Optoelectronic Performances of Multilayer MoS_2-WS_2 Heterostructure Transistors, *Adv. Funct. Mater.*, 2014, **24**(44), 7025–7031, DOI: 10.1002/adfm.201401504.

28 Y. Xue, Y. Zhang, Y. Liu, H. Liu, J. Song, J. Sophia, J. Liu, Z. Xu, Q. Xu, Z. Wang, J. Zheng, Y. Liu, S. Li and Q. Bao, Scalable Production of a Few-Layer MoS_2/WS_2 Vertical Heterojunction Array and Its Application for Photodetectors, *ACS Nano*, 2016, **10**(1), 573–580, DOI: 10.1021/acsnano.5b05596.

29 N. Choudhary, J. Park, J. Y. Hwang, H.-S. Chung, K. H. Dumas, S. I. Khondaker, W. Choi and Y. Jung, Centimeter Scale Patterned Growth of Vertically Stacked Few Layer Only 2D MoS2/WS2 van Der Waals Heterostructure, *Sci. Rep.*, 2016, **6**(1), 25456, DOI: 10.1038/srep25456.

30 T. Qi, Y. Gong, A. Li, X. Ma, P. Wang, R. Huang, C. Liu, R. Sakidja, J. Z. Wu, R. Chen and L. Zhang, Interlayer Transition in a vdW Heterostructure toward Ultrahigh Detectivity Shortwave Infrared Photodetectors, *Adv. Funct. Mater.*, 2020, **30**(3), 1905687, DOI: 10.1002/adfm.201905687.

31 J. Liu, Z. Li, X. Zhang and G. Lu, Unraveling Energy and Charge Transfer in Type-II van Der Waals Heterostructures, *npj Comput. Mater.*, 2021, **7**(1), 191, DOI: 10.1038/s41524-021-00663-w.

32 A. Balapure, J. R. Dutta and R. Ganesan, Recent Advances in Semiconductor Heterojunctions: A Detailed Review of the Fundamentals of Photocatalysis, Charge Transfer Mechanism and Materials, *RSC Appl. Interfaces*, 2024, **1**, 43, DOI: 10.1039/D3LF00126A.

33 Q. Li, N. Zhang, Y. Yang, G. Wang and D. H. L. Ng, High Efficiency Photocatalysis for Pollutant Degradation with MoS_2/C_3 N_4 Heterostructures, *Langmuir*, 2014, **30**(29), 8965–8972, DOI: 10.1021/la502033t.

34 K. Ren, K. Wang, Y. Cheng, W. Tang and G. Zhang, Two-Dimensional Heterostructures for Photocatalytic Water Splitting: A Review of Recent Progress, *Nano Futures*, 2020, **4**(3), 032006, DOI: 10.1088/2399-1984/abacab.

35 Y. Wang, Z. Ding, N. Arif, W.-C. Jiang and Y.-J. Zeng, 2D Material Based Heterostructures for Solar Light Driven Photocatalytic H_2 Production, *Mater. Adv.*, 2022, **3**(8), 3389–3417, DOI: 10.1039/D2MA00191H.

36 G. Ferrando, M. Gardella, G. Zambito, M. Barelli, D. Chowdhury, M. C. Giordano and F. Buatier de Mongeot, Flat-Optics Hybrid MoS_2/Polymer Films for Photochemical Conversion, *Nanoscale*, 2023, **15**(4), 1953–1961, DOI: 10.1039/D2NR05004H.

37 Z. Lin, Y. Huang and X. Duan, Van Der Waals Thin-Film Electronics, *Nat. Electron.*, 2019, **2**(9), 378–388, DOI: 10.1038/s41928-019-0301-7.

38 C.-H. Yeh, Z.-Y. Liang, Y.-C. Lin, T.-L. Wu, T. Fan, Y.-C. Chu, C.-H. Ma, Y.-C. Liu, Y.-H. Chu, K. Suenaga and P.-W. Chiu, Scalable van Der Waals Heterojunctions for High-Performance Photodetectors, *ACS Appl. Mater. Interfaces*, 2017, **9**(41), 36181–36188, DOI: 10.1021/acsami.7b10892.

39 C. Martella, C. Mennucci, E. Cinquanta, A. Lamperti, E. Cappelluti, F. Buatier de Mongeot and A. Molle, Anisotropic MoS_2 Nanosheets Grown on Self-Organized Nanopatterned Substrates, *Adv. Mater.*, 2017, **29**(19), 1605785, DOI: 10.1002/adma.201605785.

40 O. Song, D. Rhee, J. Kim, Y. Jeon, V. Mazánek, A. Söll, Y. A. Kwon, J. H. Cho, Y.-H. Kim, Z. Sofer and J. Kang, All Inkjet-Printed Electronics Based on Electrochemically Exfoliated Two-Dimensional Metal, Semiconductor, and Dielectric, *npj 2D Mater. Appl.*, 2022, **6**(1), 64, DOI: 10.1038/s41699-022-00337-1.

41 K. Zhu, C. Wen, A. A. Aljarb, F. Xue, X. Xu, V. Tung, X. Zhang, H. N. Alshareef and M. Lanza, The Development of Integrated Circuits Based on Two-Dimensional Materials, *Nat. Electron.*, 2021, **4**(11), 775–785, DOI: 10.1038/s41928-021-00672-z.

42 M. C. Giordano, G. Zambito, M. Gardella and F. Buatier de Mongeot, Deterministic Thermal Sculpting of Large-Scale 2D

Semiconductor Nanocircuits, *Adv. Mater. Interfaces*, 2022, 2201408, DOI: **10.1002/admi.202201408**.

43 W. Zhang, C.-P. Chuu, J.-K. Huang, C.-H. Chen, M.-L. Tsai, Y.-H. Chang, C.-T. Liang, Y.-Z. Chen, Y.-L. Chueh, J.-H. He, M.-Y. Chou and L.-J. Li, Ultrahigh-Gain Photodetectors Based on Atomically Thin Graphene-MoS2 Heterostructures, *Sci. Rep.*, 2014, **4**(1), 3826, DOI: **10.10s38/srep03826**.

44 Q. Liu, B. Cook, M. Gong, Y. Gong, D. Ewing, M. Casper, A. Stramel and J. Wu, Printable Transfer-Free and Wafer-Size MoS_2/Graphene van Der Waals Heterostructures for High-Performance Photodetection, *ACS Appl. Mater. Interfaces*, 2017, **9**(14), 12728–12733, DOI: **10.1021/acsami.7b00912**.

45 M. C. Giordano, D. Repetto, C. Mennucci, A. Carrara and F. B. Mongeot de, Template-Assisted Growth of Transparent Plasmonic Nanowire Electrodes, *Nanotechnology*, 2016, **27**(49), 495201, DOI: **10.1088/0957-4484/27/49/495201**.

46 A. Reina, H. Son, L. Jiao, B. Fan, M. S. Dresselhaus, Z. Liu and J. Kong, Transferring and Identification of Single- and Few-Layer Graphene on Arbitrary Substrates, *J. Phys. Chem. C*, 2008, **112**(46), 17741–17744, DOI: **10.1021/jp807380s**.

47 J.-B. Wu, M.-L. Lin, X. Cong, H.-N. Liu and P.-H. Tan, Raman Spectroscopy of Graphene-Based Materials and Its Applications in Related Devices, *Chem. Soc. Rev.*, 2018, **47**(5), 1822–1873, DOI: **10.1039/C6CS00915H**.

48 A. C. Ferrari, Raman Spectroscopy of Graphene and Graphite: Disorder, Electron–Phonon Coupling, Doping and Nonadiabatic Effects, *Solid State Commun.*, 2007, **143**(1–2), 47–57, DOI: **10.1016/j.ssc.2007.03.052**.

49 R. R. Nair, P. Blake, A. N. Grigorenko, K. S. Novoselov, T. J. Booth, T. Stauber, N. M. R. Peres and A. K. Geim, Fine Structure Constant Defines Visual Transparency of Graphene, *Science*, 2008, **320**(5881), 1308–1308, DOI: **10.1126/science.1156965**.

50 K.-G. Zhou, F. Withers, Y. Cao, S. Hu, G. Yu and C. Casiraghi, Raman Modes of MoS_2 Used as Fingerprint of van Der Waals Interactions in 2-D Crystal-Based Heterostructures, *ACS Nano*, 2014, **8**(10), 9914–9924, DOI: **10.1021/nn5042703**.

51 C. Mennucci, A. Mazzanti, C. Martella, A. Lamperti, M. Bhatnagar, R. Lo Savio, L. Repetto, A. Camellini, M. Zavelani-Rossi, A. Molle, F. Buatier de Mongeot and G. Della Valle, Geometrical Engineering of Giant Optical Dichroism in Rippled MoS_2 Nanosheets, *Adv. Opt. Mater.*, 2021, **9**(2), 2001408, DOI: **10.1002/adom.202001408**.

52 A. Berkdemir, H. R. Gutiérrez, A. R. Botello-Méndez, N. Perea-López, A. L. Elías, C.-I. Chia, B. Wang, V. H. Crespi, F. López-Urías, J.-C. Charlier, H. Terrones and M. Terrones, Identification of Individual and Few Layers of WS2 Using Raman Spectroscopy, *Sci. Rep.*, 2013, **3**(1), 1755, DOI: **10.1038/srep01755**.

53 V. Vega-Mayoral, D. Vella, T. Borzda, M. Prijatelj, I. Tempra, E. A. A. Pogna, S. Dal Conte, P. Topolovsek, N. Vujicic, G. Cerullo, D. Mihailovic and C. Gadermaier, Exciton and Charge Carrier Dynamics in Few-Layer WS_2, *Nanoscale*, 2016, **8**(10), 5428–5434, DOI: **10.1039/C5NR08384B**.

54 R. Ganatra and Q. Zhang, Few-Layer MoS $_2$: A Promising Layered Semiconductor, *ACS Nano*, 2014, **8**(5), 4074–4099, DOI: **10.1021/nn405938z**.

55 A. L. Elías, N. Perea-López, A. Castro-Beltrán, A. Berkdemir, R. Lv, S. Feng, A. D. Long, T. Hayashi, Y. A. Kim, M. Endo, H. R. Gutiérrez, N. R. Pradhan, L. Balicas, T. E. Mallouk, F. López-Urías, H. Terrones and M. Terrones, Controlled Synthesis and Transfer of Large-Area WS_2 Sheets: From Single Layer to Few Layers, *ACS Nano*, 2013, **7**(6), 5235–5242, DOI: **10.1021/nn400971k**.

56 Y. Zhang, D. Venkatakrishnarao, M. Bosman, W. Fu, S. Das, F. Bussolotti, R. Lee, S. L. Teo, D. Huang, I. Verzhbitskiy, Z. Jiang, Z. Jiang, J. Chai, S. W. Tong, Z.-E. Ooi, C. P. Y. Wong, Y. S. Ang, K. E. J. Goh and C. S. Lau, Liquid-Metal-Printed Ultrathin Oxides for Atomically Smooth 2D Material Heterostructures, *ACS Nano*, 2023, **17**(8), 7929–7939, DOI: **10.1021/acsnano.3c02128**.

57 B. Radisavljevic, A. Radenovic, J. Brivio, V. Giacometti and A. Kis, Single-Layer MoS2 Transistors, *Nat. Nanotechnol.*, 2011, **6**(3), 147–150, DOI: **10.1038/nnano.2010.279**.

58 N. Perea-López, Z. Lin, N. R. Pradhan, A. Iñiguez-Rábago, A. Laura Elías, A. McCreary, J. Lou, P. M. Ajayan, H. Terrones, L. Balicas and M. Terrones, CVD-Grown Monolayered MoS_2 as an Effective Photosensor Operating at Low-Voltage, *2D Mater.*, 2014, **1**(1), 011004, DOI: **10.1088/2053-1583/1/1/011004**.

59 X.-G. Zhao, Z. Shi, X. Wang, H. Zou, Y. Fu and L. Zhang, Band Structure Engineering through van Der Waals Heterostructing Superlattices of Two-Dimensional Transition Metal Dichalcogenides, *InfoMat*, 2021, **3**(2), 201–211, DOI: **10.1002/inf2.12155**.

60 J. Kang, S. Tongay, J. Zhou, J. Li and J. Wu, Band Offsets and Heterostructures of Two-Dimensional Semiconductors, *Appl. Phys. Lett.*, 2013, **102**(1), 012111, DOI: **10.1063/1.4774090**.

61 M.-Y. Li, C.-H. Chen, Y. Shi and L.-J. Li, Heterostructures Based on Two-Dimensional Layered Materials and Their Potential Applications, *Mater. Today*, 2016, **19**(6), 322–335, DOI: **10.1016/j.mattod.2015.11.003**.

62 S. Zhang, M. Maruyama, S. Okada, M. Xue, K. Watanabe, T. Taniguchi, K. Hashimoto, Y. Miyata, R. Canton-Vitoria and R. Kitaura, Observation of the Photovoltaic Effect in a van Der Waals Heterostructure, *Nanoscale*, 2023, **15**(12), 5948–5953, DOI: **10.1039/D2NR06616E**.

63 Y. Gong, J. Lin, X. Wang, G. Shi, S. Lei, Z. Lin, X. Zou, G. Ye, R. Vajtai, B. I. Yakobson, H. Terrones, M. Terrones, B. K. Tay, J. Lou, S. T. Pantelides, Z. Liu, W. Zhou and P. M. Ajayan, Vertical and In-Plane Heterostructures from WS2/MoS2 Monolayers, *Nat. Mater.*, 2014, **13**(12), 1135–1142, DOI: **10.1038/nmat4091**.

64 B. Kim, J. Kim, P.-C. Tsai, H. Choi, S. Yoon, S.-Y. Lin and D.-W. Kim, Large Surface Photovoltage of WS2/MoS2 and MoS2/WS2 Vertical Hetero-Bilayers, *ACS Appl. Electron. Mater.*, 2021, **3**(6), 2601–2606, DOI: **10.1021/acsaelm.1c00192**.

65 D. Pareek, M. A. Gonzalez, N. Grewo, M. L. Janßen, K. Arunakiri, K. L. Alimi, M. Silies, J. Parisi, L. Gütay and S. Schäfer, Large-Area Growth of MoS2/WS2 Heterostructures by a Sequential Atomic Layer Deposition and Spin-Coating Approach, *Adv. Mater. Interfaces*, 2022, **9**(31), 2200816, DOI: **10.1002/admi.202200816**.

66 M. Acar, M. Ertuğrul and E. Gür, Transfer-Free, Scalable Vertical Heterostructure FET on MoS2/WS2 Continuous Films, *Nanotechnology*, 2022, **33**(47), 475201, DOI: **10.1088/1361-6528/ac8997**.

67 V. Kaushik, M. Ahmad, K. Agarwal, D. Varandani, B. D. Belle, P. Das and B. R. Mehta, Charge Transport in 2D MoS2, WS2, and MoS2–WS2 Heterojunction-Based Field-Effect Transistors: Role of Ambipolarity, *J. Phys. Chem. C*, 2020, **124**(42), 23368–23379, DOI: **10.1021/acs.jpcc.0c05651**.

68 C.-R. Wu, X.-R. Chang, T.-W. Chu, H.-A. Chen, C.-H. Wu and S.-Y. Lin, Establishment of 2D Crystal Heterostructures by Sulfurization of Sequential Transition Metal Depositions: Preparation, Characterization, and Selective Growth, *Nano Lett.*, 2016, **16**(11), 7093–7097, DOI: **10.1021/acs.nanolett.6b03353**.

69 S. Lineykin, M. Averbukh and A. Kuperman, An Improved Approach to Extract the Single-Diode Equivalent Circuit Parameters of a Photovoltaic Cell/Panel, *Renewable Sustainable Energy Rev.*, 2014, **30**, 282–289, DOI: **10.1016/j.rser.2013.10.015**.

70 V. Sorkin, H. Zhou, Z. G. Yu, K.-W. Ang and Y.-W. Zhang, The Effects of Point Defect Type, Location, and Density on the Schottky Barrier Height of Au/MoS2 Heterojunction: A First-Principles Study, *Sci. Rep.*, 2022, **12**(1), 18001, DOI: **10.1038/s41598-022-22913-7**.

71 Y. S. Ang, L. Cao and L. K. Ang, Physics of Electron Emission and Injection in Two-Dimensional Materials: Theory and Simulation, *InfoMat*, 2021, **3**(5), 502–535, DOI: **10.1002/inf2.12168**.

72 J. Xie, N. M. Patoary, G. Zhou, M. Y. Sayyad, S. Tongay and I. S. Esqueda, Analysis of Schottky Barrier Heights and Reduced Fermi-Level Pinning in Monolayer CVD-Grown MoS2 Field-Effect-Transistors, *Nanotechnology*, 2022, **33**(22), 225702, DOI: **10.1088/1361-6528/ac55d2**.

73 W. Liu, D. Sarkar, J. Kang, W. Cao and K. Banerjee, Impact of Contact on the Operation and Performance of Back-Gated Monolayer MoS2 Field-Effect-Transistors, *ACS Nano*, 2015, **9**(8), 7904–7912, DOI: **10.1021/nn506512j**.

74 A. Pelella, O. Kharsah, A. Grillo, F. Urban, M. Passacantando, F. Giubileo, L. Iemmo, S. Sleziona, E. Pollmann, L. Madauß, M. Schleberger and A. Di Bartolomeo, Electron Irradiation of Metal Contacts in Monolayer MoS2 Field-Effect Transistors, *ACS Appl. Mater. Interfaces*, 2020, **12**(36), 40532–40540, DOI: **10.1021/acsami.0c11933**.

75 P.-C. Shen, C. Su, Y. Lin, A.-S. Chou, C.-C. Cheng, J.-H. Park, M.-H. Chiu, A.-Y. Lu, H.-L. Tang, M. M. Tavakoli, G. Pitner, X. Ji, Z. Cai, N. Mao, J. Wang, V. Tung, J. Li, J. Bokor, A. Zettl, C.-I. Wu, T. Palacios, L.-J. Li and J. Kong, Ultralow Contact Resistance between Semimetal and Monolayer Semiconductors, *Nature*, 2021, **593**(7858), 211–217, DOI: **10.1038/s41586-021-03472-9**.

76 T. Su, Y. Li, Q. Wang, W. Zhao, L. Cao and Y. S. Ang, Semimetal Contacts to Monolayer Semiconductor: Weak Metalization as an Effective Mechanism to Schottky Barrier Lowering, *J. Phys. D: Appl. Phys.*, 2023, **56**(23), 234001, DOI: **10.1088/1361-6463/acc53f**.

77 Y. Wang, J. C. Kim, R. J. Wu, J. Martinez, X. Song, J. Yang, F. Zhao, A. Mkhoyan, H. Y. Jeong and M. Chhowalla, Van Der Waals Contacts between Three-Dimensional Metals and Two-Dimensional Semiconductors, *Nature*, 2019, **568**(7750), 70–74, DOI: **10.1038/s41586-019-1052-3**.

78 C. S. Lau, J. Y. Chee, Y. S. Ang, S. W. Tong, L. Cao, Z.-E. Ooi, T. Wang, L. K. Ang, Y. Wang, M. Chhowalla and K. E. J. Goh, Quantum Transport in Two-Dimensional WS2 with High-Efficiency Carrier Injection through Indium Alloy Contacts, *ACS Nano*, 2020, **14**(10), 13700–13708, DOI: **10.1021/acsnano.0c05915**.

79 D. Monga and S. Basu, Tuning the Photocatalytic/Electrocatalytic Properties of MoS_2 / $MoSe_2$ Heterostructures by Varying the Weight Ratios for Enhanced Wastewater Treatment and Hydrogen Production, *RSC Adv.*, 2021, **11**(37), 22585–22597, DOI: **10.1039/D1RA01760H**.

80 A. Fernández-Pérez and G. Marbán, Visible Light Spectroscopic Analysis of Methylene Blue in Water; What Comes after Dimer?, *ACS Omega*, 2020, **5**(46), 29801–29815, DOI: **10.1021/acsomega.0c03830**.

81 D. James and T. Zubkov, Photocatalytic Properties of Free and Oxide-Supported MoS2 and WS2 Nanoparticles Synthesized without Surfactants, *J. Photochem. Photobiol., A*, 2013, **262**, 45–51, DOI: **10.1016/j.jphotochem.2013.04.015**.

82 C. Qin, W. Liu, N. Liu, Z. Zhou, J. Song, S. Ma, Z.-Y. Jiao and S. Lei, Observation of Hole Transfer in MoS_2/WS_2 Van Der Waals Heterostructures, *ACS Photonics*, 2022, **9**(5), 1709–1716, DOI: **10.1021/acsphotonics.2c00078**.

83 X. Hong, J. Kim, S.-F. Shi, Y. Zhang, C. Jin, Y. Sun, S. Tongay, J. Wu, Y. Zhang and F. Wang, Ultrafast Charge Transfer in Atomically Thin MoS2/WS2 Heterostructures, *Nat. Nanotechnol.*, 2014, **9**(9), 682–686, DOI: **10.1038/nnano.2014.167**.

84 Y. Shi, H. Li and L.-J. Li, Recent Advances in Controlled Synthesis of Two-Dimensional Transition Metal Dichalcogenides *via* Vapour Deposition Techniques, *Chem. Soc. Rev.*, 2015, **44**(9), 2744–2756, DOI: **10.1039/C4CS00256C**.

85 P. P. Tummala, S. Ghomi, C. S. Casari, C. Martella, A. Lamperti and A. Molle, Large Area Growth and Phase Selectivity of MoTe2 Nanosheets through Simulation-Guided CVD Tellurization, *Adv. Mater. Interfaces*, 2023, **10**(1), 2200971, DOI: **10.1002/admi.202200971**.